



ISTITUTO NAZIONALE DI RICERCA METROLOGICA Repository Istituzionale

Size-dependent catalytic effect of magnetite nanoparticles in the synthesis of tunable magnetic polyaniline nanocomposites

This is the author's accepted version of the contribution published as:

Original

Size-dependent catalytic effect of magnetite nanoparticles in the synthesis of tunable magnetic polyaniline nanocomposites / Falletta, Ermelinda; Ferretti, Anna M.; Mondini, Sara; Evangelisti, Claudio; Capetti, Elena; Olivetti, Elena Sonia; Martino, Luca; Beatrice, Cinzia; Soares, Gabriel; Pasquale, Massimo; Della Pina, Cristina; Ponti, Alessandro. - In: CHEMICKÉ ZVESTI. - ISSN 0366-6352. - 75:10(2021), pp. 5057-5069. [10.1007/s11696-021-01604-z]

Availability:

This version is available at: 11696/73570 since: 2022-02-23T17:57:04Z

Publisher:

SPRINGER INTERNATIONAL PUBLISHING AG

Published

DOI:10.1007/s11696-021-01604-z

Terms of use:

This article is made available under terms and conditions as specified in the corresponding bibliographic description in the repository

Publisher copyright
SPRINGER NATURE

This version of the article has been accepted for publication, after peer review (when applicable) and is subject to Springer Nature's AM terms of use, but is not the Version of Record and does not reflect post-acceptance improvements, or any corrections.

(Article begins on next page)

Size-dependent catalytic effect of magnetite nanoparticles in the synthesis of tunable magnetic polyaniline nanocomposites

Ermelinda Falletta^{1*}, Anna M. Ferretti², Sara Mondini², Claudio Evangelisti^{2†}, Elena Capetti², Elena Sonia Olivetti³, Luca Martino³, Cinzia Beatrice³, Gabriel Soares³, Massimo Pasquale³, Cristina Della Pina¹, Alessandro Ponti^{2*}

¹ *Department of Chemistry, University of Milan, via C. Golgi, 19, 20133, Milan (Italy)*

² *Istituto di Scienze e Tecnologie Chimiche “Giulio Natta” (SCITEC), Consiglio Nazionale delle Ricerche, via G. Fantoli 16/15, 20138, Milan (Italy)*

³ *Istituto Nazionale di Ricerca Metrologica (INRIM), Strada delle Cacce 91, 10135, Torino (Italy)*

* Corresponding author, e-mail: alessandro.ponti@scitec.cnr.it, ermelinda.falletta@unimi.it

† Present address: Istituto di Chimica dei Composti Organometallici (ICCOM), Consiglio Nazionale delle Ricerche, Via G. Moruzzi 1, 56124, Pisa (Italy)

Abstract

Nanocomposites comprising magnetic nanoparticles (NPs) embedded in an organic conducting polymer are promising materials that may allow one to exploit synergic effects between the electrically conducting and the magnetically permeable components. Having already shown that magnetite NPs can be conveniently used as a catalyst for the oxidative polymerization of the aniline dimer resulting in NPs embedded in the final composite and how to modulate the magnetic coercivity of the composites, we now turn to investigate how the size of magnetite NPs affects the polymerization and the properties of the final composite. Magnetite NPs of diameter 2.3, 10, and 27 nm turned out to be effective catalysts with cheap oxidants such as H₂O₂ and O₂. Yield data show that the rate-determining step occurs on the NP surface. Extensive characterization shows that the NPs are well-dispersed in the composite with no significant morphological change. The static magnetic properties of the composites are widely different, e. g, the magnetic blocking temperature shifts from 290 K for 27 nm NPs to 54 K for 10 nm NPs while composites with 2.3 nm NPs are virtually unblocked down to 5 K. The dynamic electromagnetic behavior studied up to the microwave range only shows energy absorptions associated to the ferromagnetic resonance, at frequencies around 1 GHz.

Keywords: Fe₃O₄, PANI, magnetic nanoparticles, catalysis, electromagnetic absorption.

Introduction

Since their discovery, intrinsically conducting polymers (CPs) have emerged as outstanding materials for numerous applications in many sectors, ranging from sensors (Wang *et al.*, 2020) to biomedicine (Kaur *et al.*, 2015) passing from organic solar cells (Dong *et al.*, 2012), environmental remediation (Ibanez *et al.*, 2018) and so on (Yang *et al.*, 2019; Li *et al.*, 2020). Among CPs, polyaniline (PANI) is unique for its ease of synthesis, low cost, biocompatibility, environmental stability, and extraordinary tunable properties (Badra *et al.*, 2009).

In recent years, materials combining characteristics and properties of two or more components have been sought and required in many sectors. Among them, PANI/Fe₃O₄ nanocomposites have been recently investigated as advanced materials being both electrically conducting and magnetically permeable and having potential application in fields such as batteries (Wang *et al.*, 2017), electromagnetic interference shielding (Movassagh-Alanagh *et al.*, 2017), environmental remediation (Muhammad *et al.*, 2019), cancer therapy (Ahmadkhani *et al.*, 2019),.

Several approaches have been developed to prepare these composites: mixing of PANI with Fe₃O₄, self-assembly method, *in situ* polymerization, ultrasonic irradiation (Qiu *et al.*, 2006). The ability of magnetite (and cobalt ferrite) nanoparticles (NPs) to act as catalysts in the PANI synthesis was explored for the first time by us in the catalytic polymerization of *N*-4-(aminophenyl)aniline (Della Pina *et al.*, 2012; Della Pina *et al.*, 2014; Della Pina *et al.*, 2015; Falletta *et al.*, 2015). Most recently, Mišurović and coworkers applied Fe₃O₄ NPs as the catalyst in the aniline polymerization (Mišurović *et al.*, 2019).

Exploiting magnetite NPs of different size to catalyze the polymerization of AD and prepare PANI/Fe₃O₄ nanocomposites would allow one to tune the magnetic properties of the composites provided that the NPs are size monodisperse and effective as a catalyst. The first requirement can be met thanks to the well-established methods of size-controlled colloidal nanochemistry (Ferretti *et al.*, 2021). As to the second one, the activity of a heterogeneous catalysts is strongly related to its particle size since it is intrinsically dependent on the surface-to-volume ratio, which dramatically grows passing from bulk to nano-dimensions. Moreover, compared to bulk materials, NPs have a larger surface density of atoms in sites, such as corner or edge sites, that maximize their reactivity because NPs are synthesized under kinetic control

and have spherical shape without the well-defined facets or crystals grown near thermodynamic equilibrium. However, because of the small dimensions, the outstanding activity of nanostructured materials is sometimes compromised by their strong interaction with intermediates and by aggregation phenomena. To the best of our knowledge, the size-dependent catalytic activity of Fe₃O₄ NPs in the oxidative polymerization of *N*-4-(aminophenyl)aniline has not yet been investigated. Here, we report our recent results in the production and characterization of conducting and magnetic PANI/Fe₃O₄ composites exploring at the same time the effect of the Fe₃O₄ NP size on their catalytic activity and the variation of the electromagnetic properties of the materials as function of the NP size.

Experimental

Materials

Chemicals

All chemicals were bought from Merck and used without any purification process. Acetone (Aldrich) was distilled over KMnO₄ and stored under argon before use in the synthesis of 2.3 nm NPs.

Synthesis of 2.3 nm magnetite NPs coated with oleic acid and derived from iron solvated metal ions (SMA).

The synthesis of Fe-SMA was carried out in a static metal vapor synthesis reactor described elsewhere (Evangelisti *et al.*, 2015) and equipped with an alumina-coated tungsten crucible heated by Joule effect with a generator with a maximum power of 2 kW. Fe-solvated metal atoms (SMA) were prepared according to a previously described procedure (Barbaro *et al.*, 2015; Campisi *et al.*, 2019). Briefly, Fe vapors generated in high vacuum ($1 \cdot 10^{-5}$ mbar) by resistive heating of an alumina-coated tungsten crucible, filled with approximately 300 mg of iron, were co-condensed at -196 °C with acetone vapor (100 mL) in the glass reactor chamber for 1 h. The reactor chamber was then warmed to the melting point of the solid matrix (ca. -95 °C), and the resulting brown Fe-solvated metal atoms (SMA) solution (95 mL) was siphoned at a low temperature into a Schlenk tube under argon atmosphere. Oleic acid (1 mL) was added to the Fe-SMA at low temperature (-40 °C) under gentle stirring, and then was left overnight at room temperature to the open air. In these conditions, a red-brown precipitate was formed, which was collected by centrifugation. The precipitate was dissolved in *n*-hexane (50 mL), precipitated with acetone (50 mL) and collected by centrifugation. This latter procedure was

repeated three times to remove the excess of oleic acid. The solid was then dispersed in toluene (75 mL). The iron content of the toluene dispersion, measured by the ICP-OES procedure described below, resulted 2.60 g/L.

105

Synthesis of 10.9 nm magnetite NPs coated with oleic acid.

The NPs were synthesized by a modification of a published procedure (Hyeon *et al.*, 2001). Oleic acid (2.68 mL, 8.51 mmol) was dissolved in dioctyl ether (12 mL) in a 100 mL three-neck round-bottom flask, equipped with condenser and thermometer, under magnetic stirring and N₂ atmosphere. The solution was subjected to three vacuum–N₂ cycles at RT and then heated to 105 °C. Three vacuum–N₂ cycles were carried out at 105 °C. Next, iron pentacarbonyl (280 µL, 2.13 mmol) was injected into the solution and the reaction mixture was heated to reflux (*ca.* 285 °C) at a rate of 3 °C/min using a programmable heating unit. The solution turned black after 50 min at reflux and was aged for an additional hour before cooling to RT. The NPs were precipitated from the reaction mixture by adding acetone (60 mL), separated by centrifugation, and dispersed in petroleum ether (45 mL). To further purify the NPs, acetone (60 mL) was added to the NP dispersion and the NPs were collected by centrifugation and dispersed in toluene (23 mL). The iron content of the toluene dispersion, measured by the UV-Vis procedure described below, was 9.7 g/L.

120

Synthesis of 26.0 nm magnetite NPs coated with oleic acid.

The NPs were synthesized by a modification of a published procedure (Park *et al.*, 2004). The metal precursor Fe(III) trioleate (FeOl₃) was synthesized as follows. Potassium oleate (5.77 g., 18 mmol) and FeCl₃·6H₂O were dissolved in a mixture of H₂O (10 mL) and EtOH (12 mL) in a 100 mL round-bottom flask under magnetic stirring and N₂ atmosphere. Hexane (21 mL) was added to the reaction mixture, which was then heated to 70 °C for 4 h. After cooling to RT, the mixture was transferred to a 100 mL separatory funnel and the aqueous phase discarded. The red-brown organic phase was washed with deionized water (2 x 10 mL) and with saturated aqueous NaCl solution (2 x 40 mL). The organic phase was evaporated under reduced pressure and the waxy red-brown FeOl₃ dried under vacuum (rotary pump) at 50 °C (oil bath) for a few hours. To synthesize the NPs, FeOl₃ (1.27 g, 1.52 mmol) and oleic acid (240 µL, 0.76 mmol) were dissolved in trioctylamine (13 mL) in a 50-mL three-neck round-bottom flask, equipped with condenser and thermometer, under magnetic stirring and N₂ atmosphere. The reaction mixture was heated to reflux (*ca.* 360 °C) at a rate of 10 °C/3 min and aged for 30 min using a programmable heating unit. After cooling to RT, the NPs were precipitated from the reaction

136 mixture by adding acetone (60 mL), separated by centrifugation, and dispersed in toluene (15
 137 mL). To purify the NPs, this procedure was repeated two more times. The iron content of the
 138 toluene dispersion, measured by the UV-Vis procedure described below, was 0.68 g/L. Such
 139 low concentration was required to ensure colloidal stability of these NPs.

140

141 *Determination of the iron content of NP dispersions*

142 ICP-OES procedure. The Fe content in SMA-derived NPs was determined by inductively
 143 coupled plasma-optical emission spectroscopy (ICP-OES) (ICAP 6300 Duo, Thermo Fisher
 144 Scientific) and an external calibration methodology. The limit of detection (LOD) calculated
 145 for iron as 5 ppb. For the analysis, the toluene dispersion of SMA-derived NPs (0.5 mL) was
 146 heated in a porcelain crucible over a heating plate and the solvent was evaporated. The solid
 147 residue was dissolved in aqua regia (2 mL), heated until complete evaporation and the solid
 148 residue was then dissolved in 0.5 M aqueous HCl. The iron content was then measured by ICP-
 149 OES.

150 UV-Vis procedure. This procedure is described in detail in (Mondini *et al.*, 2015) and is here
 151 briefly outlined. About 0.1 mL of toluene NP dispersion is dissolved in aqua regia and
 152 evaporated. The residue is re-dissolved in 0.1 M HCl and the solution is buffered with PBS (pH
 153 7). The solution is then treated with tiron in excess to form the red iron complex $[\text{Fe}(\text{tiron})_3]^{3-}$
 154 that is spectrophotometrically determined by a calibration method.

155

156 *PANI/Fe₃O₄NPs composites preparation using H₂O₂ as the oxidant*

157 500 mg of *N*-4-(aminophenyl)aniline (aniline dimer, AD) were dispersed in 30 mL of water
 158 acidified with 2.7 mL of HCl 1 M (AD/HCl = 1, molar ratio). The mixture was stirred for 30
 159 minutes. Then, 1.2 mL of an aqueous of H₂O₂ 35% was added (H₂O₂/AD = 5, molar ratio,
 160 followed by different amounts of Fe₃O₄ NPs. After 24 h, a dark green solid was recovered by
 161 filtration, washed with water and acetone abundantly until clearness of the mother liquors and
 162 dried in an oven at 60°C until it reached a constant weight.

163

164 *PANI/Fe₃O₄NPs composites preparation using O₂ as the oxidant*

165 500 mg of *N*-4-(aminophenyl)aniline (aniline dimer, AD) were dispersed in 30 mL of water
 166 acidified with 2.7 mL of HCl 1 M (AD/HCl = 1, molar ratio). The mixture was stirred for 30
 167 minutes and then different amounts of Fe₃O₄ NPs were added. The reaction mixture was stirred
 168 under pressure of molecular oxygen (3 bar) for 72 h at 80°C. Finally, a dark green solid was

recovered by filtration, washed with water and acetone abundantly until clearness of the mother liquors and dried in an oven at 60°C until it reached a constant weight.

171

172 *Materials Characterization*

The TEM images, electron diffraction (ED) patterns, Electron Energy Loss Spectroscopy (EELS) data, and Energy Filtered (EF-TEM) TEM images were recorded by a ZEISS LIBRA 200FE TEM that operates at 200kV and is equipped with a second generation in-column Ω filter and a HAADF detector for STEM imaging. The samples were prepared by dropping 7 μ l of NP dispersion on a copper grid coated with a 1-3 nm carbon film and letting it dry overnight. The magnetite NPs were colloiddally dispersed in toluene, whereas the composite samples were suspended in isopropanol. TEM and EF-TEM Images were processed by means of the iTEM TEM Imaging Platform software (Olympus) and the NP size distribution was measured by the software PEBBLES (Mondini, *et al.*, 2012).

FT-IR spectra of composites were recorded in the transmittance mode in the range 500-4000 cm^{-1} at 64 scans per spectrum and a 2 cm^{-1} resolution by JASCO FT/IR-410 spectrophotometer (JASCO Corporation, Tokyo, Japan). A small amount of each sample was dispersed in KBr and compressed in 13 mm diameter pellets with a 10-ton hydrostatic press for 15 min.

X-ray powder diffraction (XRPD) analyses were carried out in a 2θ range between 10° and 80° on a Philips PW 3710 Bragg-Brentano goniometer (Philips, Amsterdam, Netherlands) equipped with a scintillation counter, a slit with 1° divergence, a receiving slit of 0.2 mm and a 0.04° Soller slit system. A graphite-monochromatic Cu K α radiation was adopted at a nominal X-ray power of 40 kV \times 40 mA.

The metal loss in the Fe₃O₄/PANI composites was determined by atomic absorption spectroscopy on a AAnalyst 100 PerkinElmer instrument.

Magnetization measurements of composites synthesized using H₂O₂ were carried out by a Quantum Design MPMS XL-5 SQUID magnetometer. Weighted amounts of composite were sealed in Teflon tape. Field-cooled (FC) and zero-field-cooled (ZFC) magnetization curves were recorded in the 5-300 K range. After cooling the sample from 300 to 5 K in zero field, the ZFC magnetization was recorded on heating to 300 K using a measuring field $H_{\text{meas}} = 10$ Oe. Next, the FC magnetization was measured ($H_{\text{meas}} = 10$ Oe) while cooling the sample from 300 to 5 K under $H_{\text{cool}} = 10$ Oe. In the case of the sample with the largest NPs (PANI/NP27), the highest temperature was set to 350 K. Magnetization isotherms (hysteresis loops) were recorded between +50 kOe and -50 kOe at 5 K after cooling in zero magnetic field. All data were corrected for the diamagnetism of the sample holder and PANI and then scaled to the NP mass.

The ac magnetic properties were determined using an Agilent 4395A impedance analyzer using a coaxial short 16454A magnetic material test fixture, and a test of the dielectric properties was performed using a parallel plate method with the 16453A dielectric material test fixture.

206

207

208

Results and discussion

Magnetite nanoparticles

To study how the NP size affects the catalytic polymerization of AD and the properties of the resulting nanocomposite, we prepared magnetite NPs of different size by different procedures, each yielding NPs with good size dispersity and uniform shape. We used thermal decomposition to prepare medium and large NPs (Hyeon *et al.*, 2001; Park *et al.*, 2004), whereas very small NPs were synthesized by metal vapor synthesis technique (Barbaro *et al.*, 2015; Campisi *et al.*, 2019). TEM images of the NP samples are reported in Figure 1. We obtained the NP morphological parameters by analyzing the TEM images using the Pebbles software (Mondini, *et al.*, 2012) and collected them in Table 1 (The histograms of the NP diameter can be found in the ESI) The three NP samples have largely different size: the diameters span more than an order of magnitude (2.3 to 27 nm) while the surface (related to the catalytic activity) and the volume (related to the magnetic properties of the composite) span more than two and three orders of magnitude, respectively. The size dispersion is good to excellent. The 28% dispersion of NP2 may seem large but one should note that the standard deviation of 0.64 nm is smaller than the magnetite cell size (0.84 nm). All NPs have spherical shape, except for the largest nanoparticles in NP27 that display cuboidal shape (see ESI for further TEM images of NP27). The crystal phase of the NP27 and NP10 samples was confirmed to be spinel (cubic ferrite) by ED (see ESI). No diffraction ring can be seen in the ED pattern of NP2 NPs. As already reported (Barbaro *et al.*, 2015), such small NPs are crystalline, and the absence of diffraction rings can then be ascribed to the very wide breadth of the rings. Finally, we note that in this paper, for the sake of clarity, we use the term “magnetite” or “Fe₃O₄” NPs to indicate iron oxide NPs with cubic ferrite crystal structure and composition Fe_{3-x}O_{4-x} (0 ≤ x ≤ 1), varying between magnetite and maghemite.

232

233

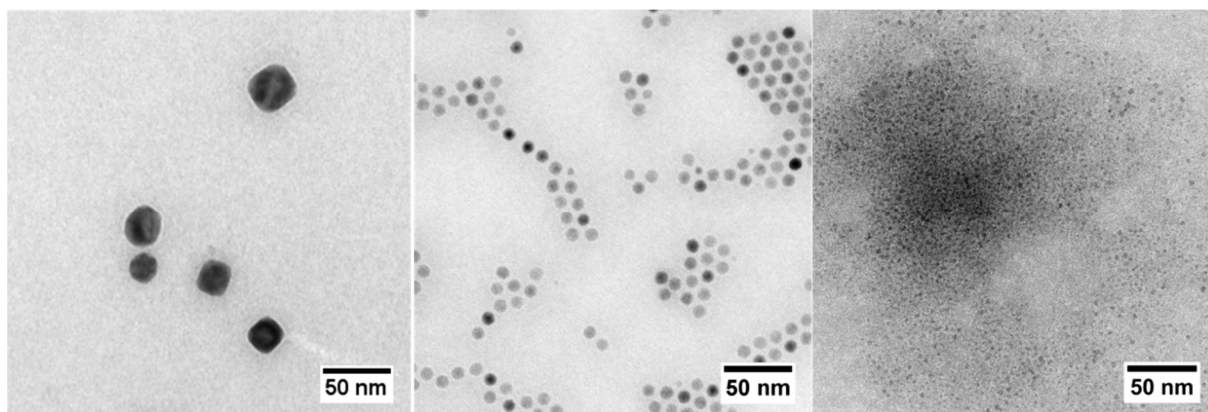


Figure 1. TEM images of as synthesized NPs. a) NP27, b) NP10 c) NP2.

Table 1. Parameters of the distribution of the diameter of as-synthesized magnetite NPs. The number of measured NPs N is reported along with the mean, standard deviation, and variation coefficient of the diameter distribution.

Sample	N	Mean (nm)	Standard deviation (nm)	Variation coefficient (%)
NP2	463	2.3	0.64	28
NP10	1417	10.0	0.43	4.3
NP27	181	27.1	4.3	16

Polymerization of AD in the presence of Fe_3O_4 nanoparticles

The dependence of the catalytic activity of Fe_3O_4 NPs on their size was evaluated in the AD oxidative polymerization. The catalytic performance of the NPs is assessed keeping in mind that the NPs are both the catalyst and the magnetic load.

In Figure 2 the yield (mass %) of composites PANI/ Fe_3O_4 NPs is plotted versus the NP/AD molar ratio, where the numerator is the amount of Fe_3O_4 contained in the NPs.

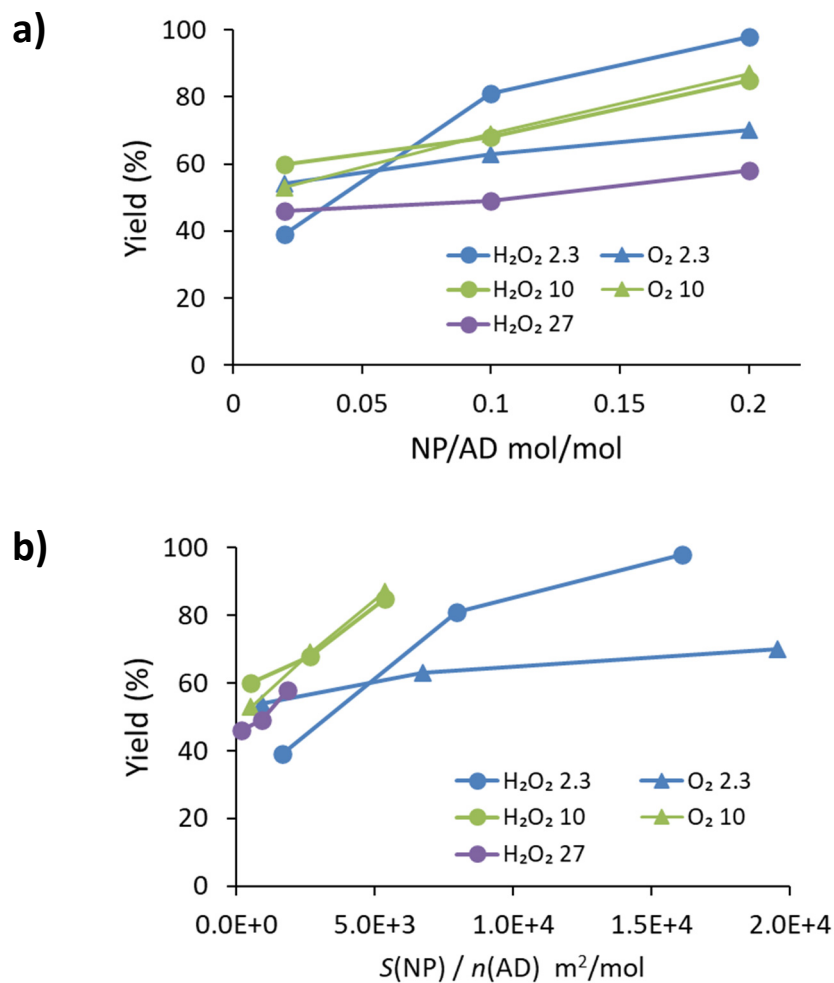


Figure 2. Yield (mass %) of composite from the AD polymerization in the presence of magnetite NPs. The yield is plotted as a function of (a) the NP/AD molar ratio and (b) the ratio of the NP surface area S to the molar amount n of AD.

253

The NP/AD molar ratio was chosen so to explore a NP/AD range that would reasonably yield composites with the desired electrical and magnetic properties. As previously reported, the oxidant used for the polymerization reaction (H₂O₂ or O₂) does not significantly affect the properties of the PANI/Fe₃O₄ composites (Della Pina *et al.*, 2012). Because H₂O₂ is especially attractive for the liquid-phase oxidation, due to the high percentage of active oxygen and the production of water as only by-product, we here focused on composites obtained using H₂O₂. Polymerizations carried out using O₂ as the oxidant are included for comparison.

In all experimental conditions explored, the yield increases with the amount of NPs, confirming the catalytic role of the NPs. More insight can be gained when the yield is plotted as a function of the ratio $S/n(AD)$, where S is the total core surface area of the NPs and $n(AD)$ is the molar amount of AD (Figure 2b). The area S is estimated from the total mass of Fe₃O₄ in the composite

265 m and their mean surface area $\langle s \rangle$ and volume $\langle v \rangle$ measured from TEM images as $S = m \langle s \rangle$
 266 $/ \rho \langle v \rangle$, where $\rho = 5.17 \text{ g/cm}^3$ is the density of magnetite. When small NP2 are used, a
 267 significant fraction of the NPs is not embedded in the final composite (see ESI). We corrected
 268 the data for NP2 in Figure 2b by considering the surface of embedded NPs only. The lack of
 269 smallest NPs can be attributed to their very high surface area that makes them more sensitive
 270 to the environment. The stability of such small particles is difficult to study and aggregation
 271 and dissolution phenomena have to be considered.

272 The yield vs. $S/n(\text{AD})$ data for the larger NPs (NP10 and NP27) is scarcely affected by the NP
 273 size or oxidant. They cluster along a straight line, indicating that the slow initial steps of the
 274 polymerization (Tzou and Gregory, 1992) occur on the surface of the NP inorganic core. This
 275 linear behavior extends to high conversion, suggesting that the NPs are stable against
 276 aggregation in the reaction conditions.

277 The yield of NP2 is always lower than that of the larger NPs. When H_2O_2 is used as an oxidant,
 278 the yield data of NP2 is parallel to that of the larger NPs but shifted to the right (Figure 2b).
 279 This suggests that partial NPs aggregation occurs during the polymerization, as confirmed by
 280 TEM (see Figure 4 below), thus decreasing the available active sites for the AD oligomerization
 281 and hindering transport of AD to them. When $\text{NP/AD} = 0.2 \text{ mol/mol}$, parallelism is lost as the
 282 yield levels off because most of the AD has undergone polymerization. When NP2 are used
 283 with O_2 , the yield at $\text{NP/AD} = 0.02 \text{ mol/mol}$ is comparable to that of the larger NPs showing
 284 that the NP surface is as active as in the other cases. However, the yield increases very slowly
 285 with the $S/n(\text{AD})$ ratio. We admit that we could not find a better explanation for this behavior
 286 than invoking extensive NP aggregation when the NP/AD ratio is larger than 0.02 and O_2 is
 287 used as an oxidant.

288 In summary, magnetite NPs with size from 2.3 to 27 nm are able to catalyze the polymerization
 289 of AD, using either H_2O_2 or O_2 as oxidant, and with yield ranging from 39% to 98%. It is
 290 therefore feasible to produce magnetic PANI composites with magnetite NPs spanning a size
 291 range wider than an order of magnitude.

292

293 *PANI/Fe₃O₄NPs characterization*

294 All composites were characterized by different techniques in order to investigate the effect of
 295 the presence of the magnetic NPs in the final materials. Here, we report the results obtained for
 296 the composites synthesized in the presence of H_2O_2 as the oxidant and using a NP/AD molar
 297 ratio of 0.2, because they are the most representative. These three composites are named
 298 PANI/NP2, PANI/NP10, and PANI/NP27.

299 The amount of magnetic NPs inside the composites was indirectly evaluated by the analysis of
 300 iron in the mother liquors obtained after the filtration of the materials. The results show that
 301 only for the composite PANI/NP2 the content of NPs within the polymeric matrix is not
 302 quantitative (16% of Fe_3O_4 , cfr. ESI). In all other cases, during the polymerization reaction the
 303 inorganic component is completely embedded in the polymeric matrix (33% of Fe_3O_4 in
 304 PANI/NP10, 31% of Fe_3O_4 in PANI/NP27).

305

306 *Fourier-transform infrared (FT-IR) spectroscopy*

307 All composites comprise a polymeric matrix consisting of PANI in the form of conducting
 308 emeraldine, as shown by characteristic infrared bands (see ESI). In particular, the broad band
 309 between $3400\text{--}1800\text{ cm}^{-1}$ confirms that the polymer was obtained in highly conjugated form
 310 (Šeděnková *et al.*, 2008), the band at 1570 and 1490 cm^{-1} are assigned to the C=C stretching
 311 vibration of quinoid and benzenoid rings respectively, whereas C-N stretching vibration is
 312 responsible of the band at 1304 cm^{-1} (Cionti *et al.*, 2020). The band at 1240 cm^{-1} is due to C-
 313 $\text{N}^{+\bullet}$ stretching vibration (Šeděnková *et al.*, 2008) and that to 1146 cm^{-1} derives from Q= NH^+ -
 314 B, B- NH^+ -B stretching (Mišurović *et al.*, 2019). C-H out-of-plane bending vibrations of 1,4-
 315 disubstituted aromatic rings lead to the bands in the $820\text{--}800\text{ cm}^{-1}$ range (Socrates, 2004).
 316 Finally, the two bands at 800 and 759 cm^{-1} suggest the presence of C-H vibrations of 1,2,4-
 317 trisubstituted and 1,2-disubstituted rings (Socrates, 2004).

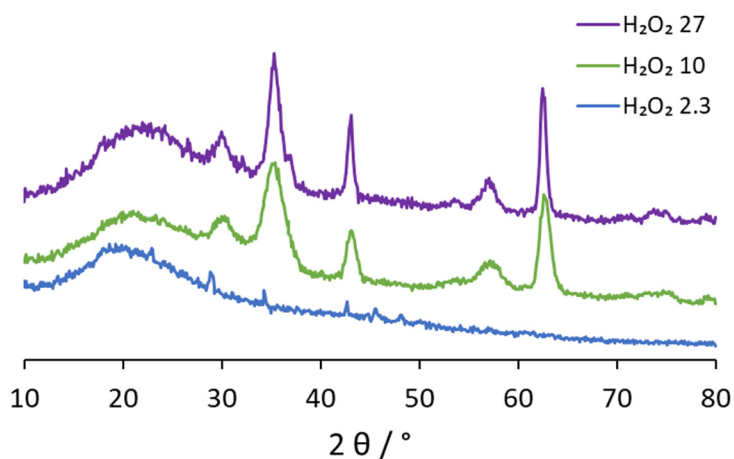
318

319 *X-ray powder diffraction (XRPD)*

320 The XRPD patterns of PANI/ Fe_3O_4 NPs composites are reported in Figure 3.

321

322



323

Figure 3. XRPD patterns of PANI/Fe₃O₄NPs composites.

324

325

326 The XRPD patterns of the composites show the typical Bragg diffraction peak at $2\theta \approx 20^\circ$ for
327 the polymer. Peaks at $2\theta = 30.1, 35.6, 43.2, 53.8, 57.2,$ and 63.0° are prominent in the patterns
328 of composites including NP10 and NP27. They can be assigned to cubic ferrite (spinel) NPs,
329 showing that during the synthesis of the composites the magnetic NPs were embedded into the
330 polymer. The XRPD pattern of PANI/NP2 composites only shows the peak of PANI. Since the
331 presence of small NP2 in the composite is established by TEM techniques (see the net section),
332 the absence of the peaks typical of the spinel structure could be due to the amorphousness of
333 the NPs. However, NP2 were already shown to be crystalline (Barbaro *et al.*, 2015). Therefore,
334 the inability to detect the spinel peaks is ascribed to combined effect of the larger peak width
335 expected for smaller NPs (about fourfold wider than for PANI/NP10) and the lower magnetite
336 content in PANI/NP2.

337

338 *TEM microscopy*

339 The TEM investigation of the composites has two goals: to establish the presence of magnetite
340 NPs within the composites and to ascertain whether the NPs underwent morphological changes
341 during the polymerization reaction. The investigation could not rely on conventional TEM
342 imaging only because the composite granules are thick enough to be opaque to the electron
343 beam except for the very edges of the granules (see ESI).

344

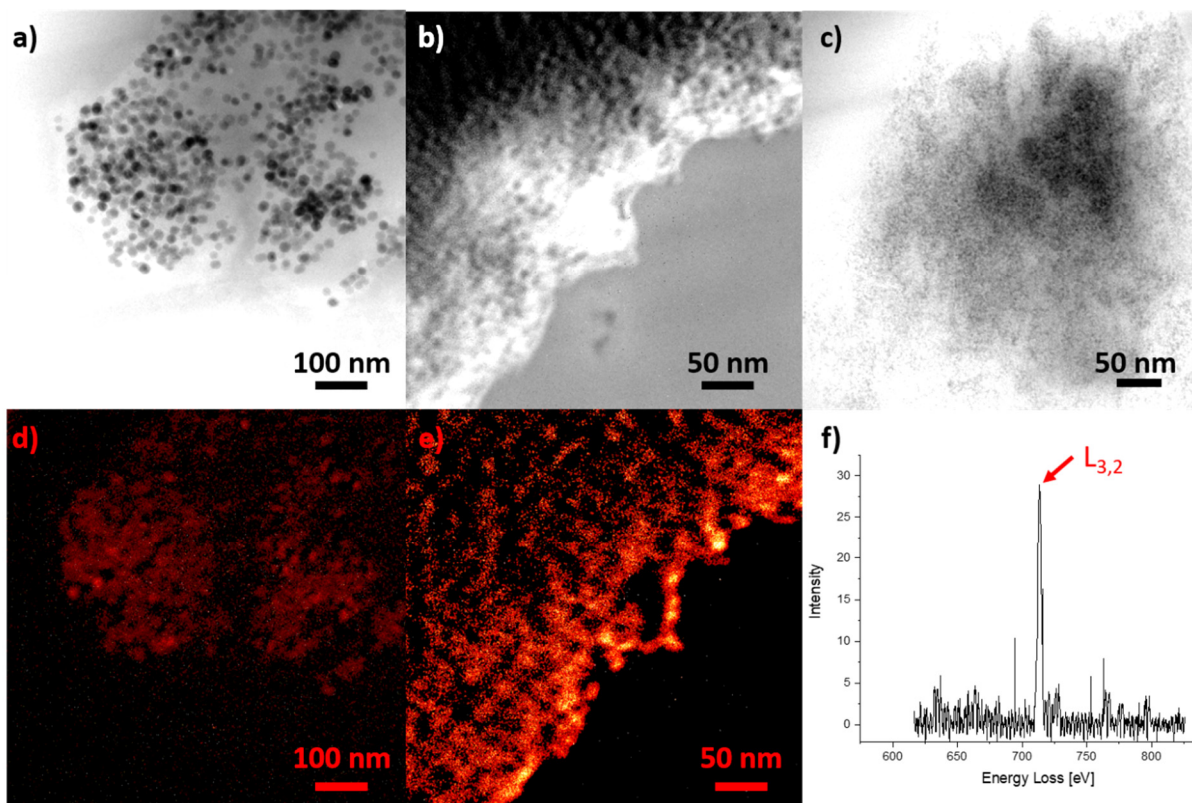


Figure 4. TEM of PANI/Fe₃O₄NPs composites. EF-TEM images filtered at 30 eV of a) PANI/NP27, b) PANI/NP10, and c) PANI/NP2. False-color EF-TEM images filtered at 713 eV providing Fe maps of d) PANI/NP27 and e) PANI/NP10. The sample regions imaged are the same as in a) and b). f) Background-subtracted EELS spectrum of PANI/NP2 showing the iron $L_{3,2}$ peak.

We thus resorted to energy-filtered TEM (EF-TEM) techniques by which the image is formed by detecting electrons that lost energy during the interaction with sample (Figure 4). In images filtered at 30 eV loss, the contrast between NPs and polymer is enhanced since electrons can lose 30 eV only by interacting with nearly-free aromatic π electrons, the so-called plasmonic mode, so that the polymer matrix appears light gray whereas the NPs appear dark. The enhanced contrast between NPs and polyaniline allowed us to identify the NPs inside the composite (Figure 4a-c). The NPs are well dispersed within the composites. Some NP agglomeration was observed in the case of the PANI/NP2 (dark region in Figure 4c). NP measurement was unfortunately reliable only for PANI/NP10 and PANI/NP27. The results are collected in Table 2. Comparing this data with those in Table 1, one can see that the NP10 are unchanged while the NP27 decreased in size by about 2 nm during the polymerization. In both cases, the size

dispersion is unchanged. We can therefore expect that the properties of the magnetic NPs are unaffected by the polymerization, except for what relates to the interparticle distance.

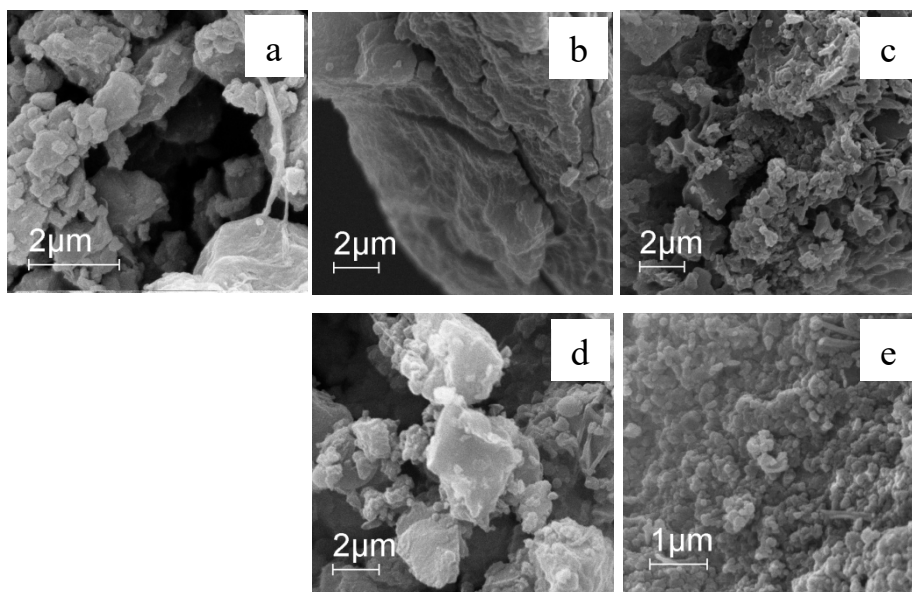
Table 2. Parameters of the distribution of the diameter of magnetite NPs present in PANI/Fe₃O₄NPs composites. The number of measured NPs N is reported along with the mean, standard deviation, and variation coefficient of the diameter distribution.

Composite	N	Mean (nm)	Standard deviation (nm)	Variation coefficient (%)
PANI/NP10	335	10.2	0.63	6.2%
PANI/NP27	207	25.0	4.6	18%

We also confirmed the presence of iron in the embedded NPs detecting electrons with energy loss of 713 eV, typical of iron ($L_{2,3}$ peak). The EF-TEM iron maps of PANI/NP27 and PANI/NP10 (Figure 4d,e) show that the iron signal coincides with the NPs as seen in the corresponding 30 eV loss images (Figure 4a,b). In the case of PANI/NP2, the intensity of the EF-TEM iron map was too low to reliably identify the NPs within the composite. The presence of iron in PANI/NP2 was established thanks to the EELS spectrum that displays the iron $L_{3,2}$ peak at 713 eV (Figure 4f). The crystal structure of the embedded NPs was analyzed by ED (see ESI): the ED patterns confirmed that PANI/NP27 and PANI/NP10 comprise cubic ferrite NPs. PANI/NP2 gave no detectable diffraction rings.

SEM microscopy

In Figure 5, SEM images of PANI/Fe₃O₄NPs composites are displayed.



383

384 **Figure 5.** SEM images of PANI/Fe₃O₄NPs composites (a: PANI/NP27, b: PANI/NP10, c:
385 PANI/NP2) or O₂ as oxidant (d: PANI/NP10, e: PANI/NP2).

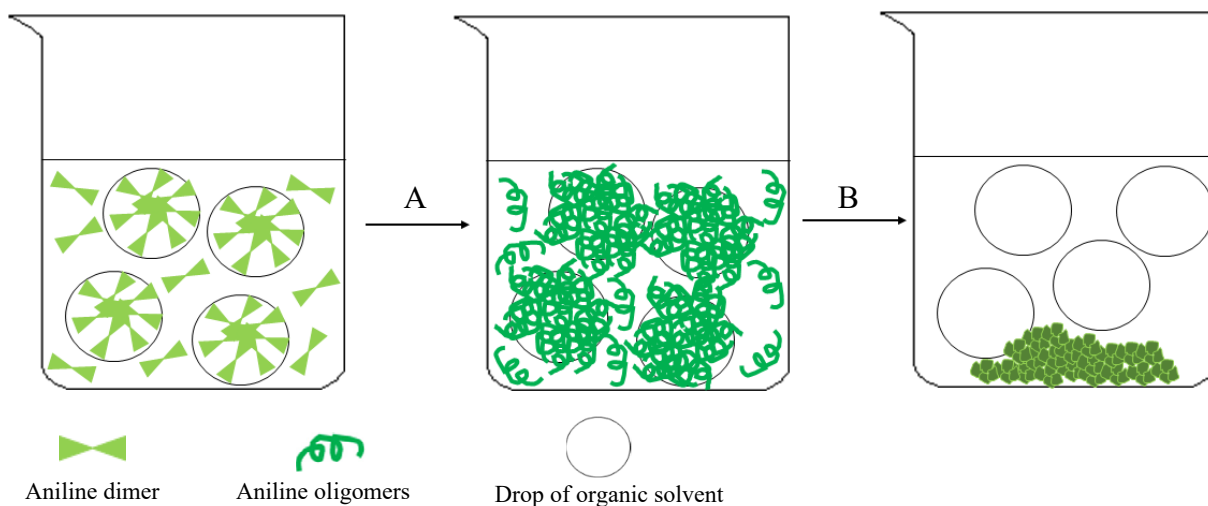
386

387 When compared to PANI obtained by the oxidative polymerization of AD in the presence of a
388 homogeneous catalyst, e.g., Fe(III) (Della Pina *et al.*, 2018), PANI/Fe₃O₄NPs composites
389 display a more globular morphology, sparsely intermixed with nanorods. As previously
390 reported (Della Pina *et al.*, 2012), when AD hydrochloride is polymerized by H₂O₂ in water in
391 the presence of magnetite NPs dispersed in an organic phase as the catalyst, an interfacial
392 polymerization occurs. Thanks to its solubility in organic solvents, AD hydrochloride can
393 diffuse into the organic phase where Fe₃O₄ NPs are present, and the oxidative polymerization
394 can take place at the interface between the organic and aqueous phases (Scheme 1).

395

396

397



Scheme 1. Proposed mechanism of nanoglobules formation. A) oligomerization step, B) polymerization step.

During the first steps of the reaction, only PANI oligomers are produced that are soluble in organic solvents and, as a consequence, they can diffuse inside the toluene drops. When the polymeric chains grow longer, they become insoluble and precipitate from the reaction mixture leading to globular materials.

Even though this hypothesis of mechanism seems to be in contrast with that previously reported (Della Pina *et al.*, 2012), it has to be considered that the amount of organic phase was changed and the catalysts were obtained by a different synthetic approach (co-precipitation reaction in Della Pina *et al.*, 2012, thermal decomposition here).

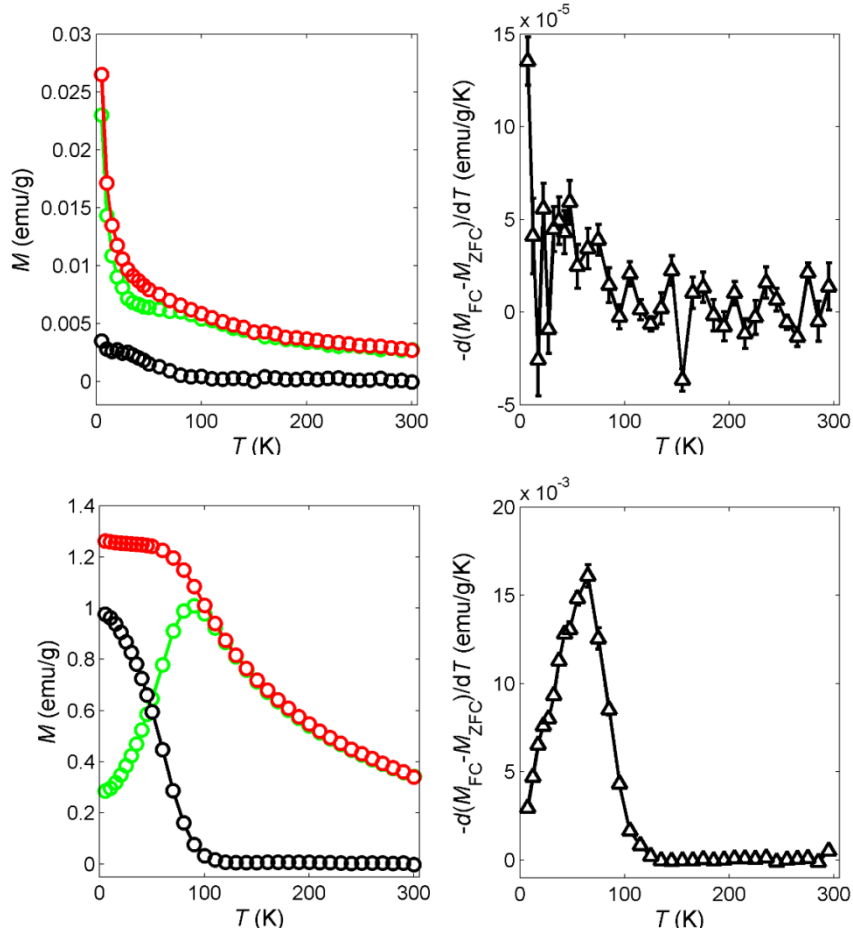
Magnetic properties

The thermal behavior of the magnetization M of the PANI/Fe₃O₄NPs composites (oxidant: H₂O₂; NP/AD = 0.02 mol/mol) was investigated by means of ZFC/FC experiments (Figure 6). The main magnetic parameters are collected in Table 3. The ZFC/FC curves of the composites are widely different. Reversible behavior is indicated by the identity of the ZFC and FC data, which is clearly visible in the high temperature range for all composites. The reversibility corresponds to the superparamagnetic (SPM) regime where thermal agitation quickly flips the NP magnetization. Upon cooling the two curves diverge as soon as thermal agitation is not able to overcome the barrier for magnetization reversal of some NPs and irreversibility sets in. The irreversibility temperature T_{irr} , defined as the temperature at which the difference between the FC and the ZFC magnetization $(M_{FC} - M_{ZFC})/M_{FC} = 3\%$, is larger than RT for PANI/NP27, as low as 110 K for PANI/NP10, and probably less than 80 K for PANI/NP2 (in the latter case,

the smallness of $M_{FC}-M_{ZFC}$ prevents an accurate determination of T_{irr}). Thus, PANI/NP27 contains NPs both in the SPM and blocked regime even at RT, in agreement with the ideal RT blocking diameter of magnetite (26 nm) (Coey, 2010).

Table 3. Magnetic parameters of the ZFC/FC magnetization of PANI/Fe₃O₄NPs composites.

Composite	T_{irr} (K)	T_{der} (K)	HWHH	
			(K)	$\langle T_b \rangle$ (K)
PANI/NP2	< 80 K	—	—	—
PANI/NP10	110	60	29	54
PANI/NP27	310	250	41	290



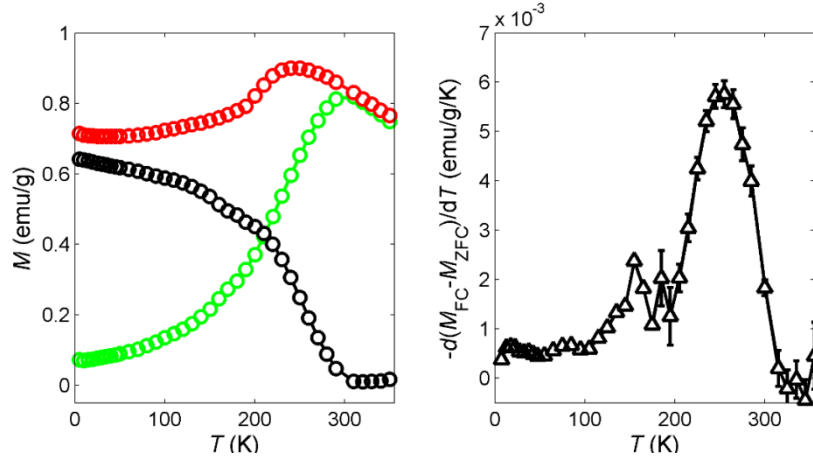


Figure 6. Thermal behavior of the low-field ($H = 10$ Oe) magnetization of PANI/Fe₃O₄NPs composites. In the left panels, the ZFC (green) and FC (red) magnetizations are shown along with their difference (black). In the right panels, the $-d(M_{FC}-M_{ZFC})/dT$ derivative is plotted to represent the distribution of the blocking temperatures. Top: PANI/NP2, middle: PANI/NP10, bottom: PANI/NP27. The error bars represent 1 standard deviation; the error bars are not visible when the standard deviation is smaller than the symbol size.

Upon further cooling below T_{irr} , more NPs enter the blocked regime. In this temperature region, the three samples display largely different behavior. M_{FC} and M_{ZFC} of PANI/NP2 are similar down to 5 K, showing that the NPs in this composite are subject to low barriers for magnetization rotation, as expected for very small NPs. PANI/NP10 displays a strong decrease of M_{ZFC} and a flattening of M_{FC} at low temperature. The larger difference between M_{FC} and M_{ZFC} corresponds to larger barriers. The M_{FC} and M_{ZFC} of PANI/NP10 and PANI/NP2 are typical of weakly interacting NPs. In the case of PANI/NP27, both M_{FC} and M_{ZFC} decrease from 250 K down to 5 K, showing strong interparticle interactions and the onset of a frozen spin-glass-like state where the magnetization is frozen in one of the many minima of a complex free-energy landscape created by the magnetostatic interaction among the NPs. The presence and freezing temperature of the spin-glass-like state agree with an estimate of the relative strength of the magnetostatic interaction among the NPs (see ESI).

A representation of the magnetization rotation barriers of a composite (in terms of blocking temperature T_b) can be obtained as the derivative of the difference between the FC and ZFC magnetization $-d(M_{FC}-M_{ZFC})/dT$ (Figure 6, right panels) (Bruvera *et al.*, 2015). This representation faithfully displays the distribution of T_b in the case of weakly-interacting NPs. When a spin-glass-like state sets in, the concept of T_b of individual NPs is not appropriate but $-d(M_{FC}-M_{ZFC})/dT$ however provides useful information about the barriers, (Woińska *et al.*,

2013) though they are a property of the whole sample and cannot be tied to individual NPs. The mode T_{der} and half-width-half-height (HWHH) of the T_{b} distribution can be found in Table 3 along with the mean barrier $\langle T_{\text{b}} \rangle$. PANI/NP2 has barriers with $T_{\text{b}} < 80$ K but T_{der} and $\langle T_{\text{b}} \rangle$ could not be reliably determined. These barriers, which are related to a small part of the total magnetization, as shown by the $M_{\text{FC}} - M_{\text{ZFC}}$ difference, can be attributed to a few NP aggregates. The barriers in PANI/NP10 are distributed about $T_{\text{der}} = 60$ K ($\langle T_{\text{b}} \rangle = 54$ K) and extend down from 100 K (HWHH 29 K). A similar peak is observed in the PANI/NP27 T_{b} distribution, but it occurs at higher $T_{\text{der}} = 250$ K ($\langle T_{\text{b}} \rangle = 290$ K) with HWHH = 41 K. The barrier distribution has a broad tail extending down to 5 K, which is related to collective barriers in the frozen state. The T_{b} of our composites agree with the T_{b} measured for magnetite NPs in the $d = 10\text{-}20$ nm range (Yun *et al.*, 2014) (see ESI for a detailed comparison).

To gain more insight into the magnetic properties of the composites, magnetization isotherms were measured between -50 and $+50$ kOe at 5 K. The shape of these hysteresis loops (see ESI) and the magnetic parameters collected in Table 4 confirm the almost complete magnetic reversibility of PANI/NP2 at low temperature and the irreversible behavior of PANI/NP10 and PANI/NP27.

In summary, these composite materials display a variety of magnetic behavior that can be selected by choosing the NP size, e.g., the SPM regime can be shifted from RT to $T \approx 5$ K.

Table 4. Magnetic parameters from the magnetization isotherm of PANI/Fe₃O₄NPs composites. The isotherms were measured between -50 and $+50$ kOe at 5 K.

Composite	M_{50} (emu/g) ^{a,b}	M_{rem} (emu/g) ^a	M_{rem} / M_{50}	H_{c} (kOe)
PANI/NP2	55.2 ± 0.8	—	—	—
PANI/NP10	53.4 ± 0.7	12.8 ± 0.2	0.24 ± 0.02	0.45
PANI/NP27	42 ± 1	6.2 ± 2	0.15 ± 0.04	0.61

^a Mass magnetization referred to the NP mass. ^b The magnetization at 50 kOe (M_{50}) is far from the saturation value.

Dynamic electromagnetic absorption and Ferromagnetic resonance

Magnetic materials subjected to an external applied field may show losses attributed to different phenomena, also frequency dependent. In quasi static conditions, losses are dominated by the hysteresis loss associated to the reversal of the magnetization direction which occurs whenever a portion of a domain wall moves between different pinning sites corresponding to two local

energy minima and some energy is dissipated to the crystal lattice. Dynamic losses due to the flow of eddy currents and joule heating within the material under ac excitations are associated to the magnetic flux variations. At higher frequencies, when flux penetration may be reduced due to the skin effect, energy dissipation is caused by ferromagnetic resonance, occurring whenever the frequency of the external ac magnetic field coincides to the Larmor precession frequency of the magnetization vector. These effects tend to limit the useful frequency range of magnetic materials in practical devices.

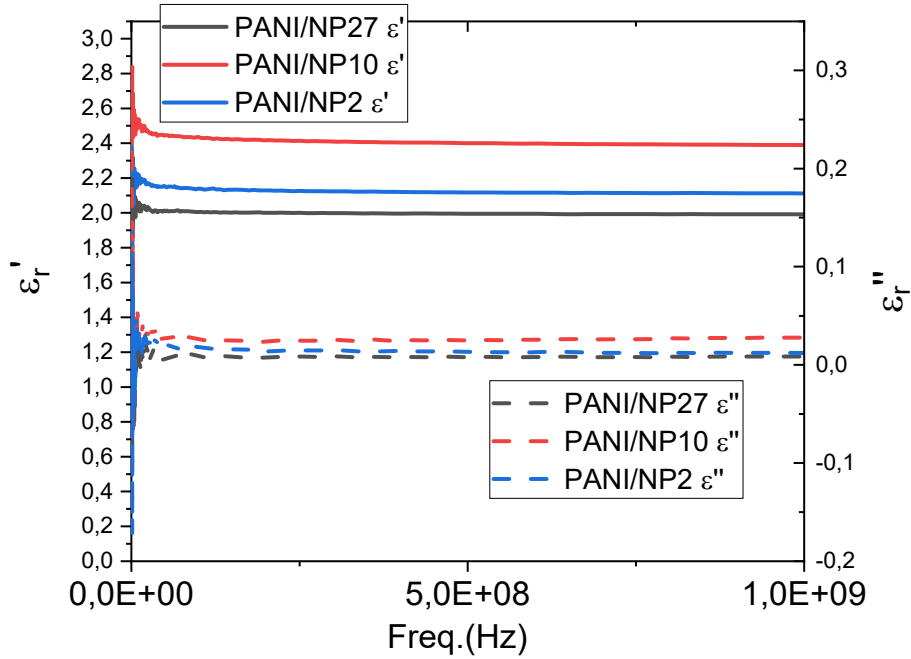
Due to their extremely small size, nanosized objects such as NPs do not exhibit large hysteresis or dynamic losses and can thus be suitable as inductors even above the MHz frequency range. In fact, NPs with diameters of the order of 10 nm are single domain and magnetization reversals occur only through rotations, which produce very small dissipation with respect to hysteresis. Dynamic losses due to large scale eddy currents are also suppressed in NPs, because inter-particle conduction is hindered by the organic shell and losses arise at frequencies above 1 GHz only due to the resonant magnetic behavior, and to verify this hypothesis dielectric characterization was also performed up to the GHz range.

The real and imaginary part of the magnetic permeability using the following relations (Fiorillo, 2010):

$$\mu' = 1 + \frac{\text{Im}\{\Delta Z_{in}^*\}}{f\mu_0 h \ln \frac{R_m}{r_m}} \quad (1)$$

$$\mu'' = \frac{\text{Re}\{\Delta Z_{in}^*\}}{f\mu_0 h \ln \frac{R_m}{r_m}} \quad (2)$$

where h , R_m and r_m are the thickness, the outside diameter, and the inside diameter of the ring sample, respectively, $\Delta Z_{in}^* = Z_{in,sample}^* - Z_{in,air}^*$, where $Z_{in,sample}^*$ and $Z_{in,air}^*$ are the circuit impedances in the presence or absence of the toroidal sample and f is the frequency. Capacitance and dielectric properties were determined directly and calibrated through a Teflon reference, and show that the dielectric properties are constant across the spectrum observed up to above 1 GHz, without any visible resonant absorption (Figure 7).



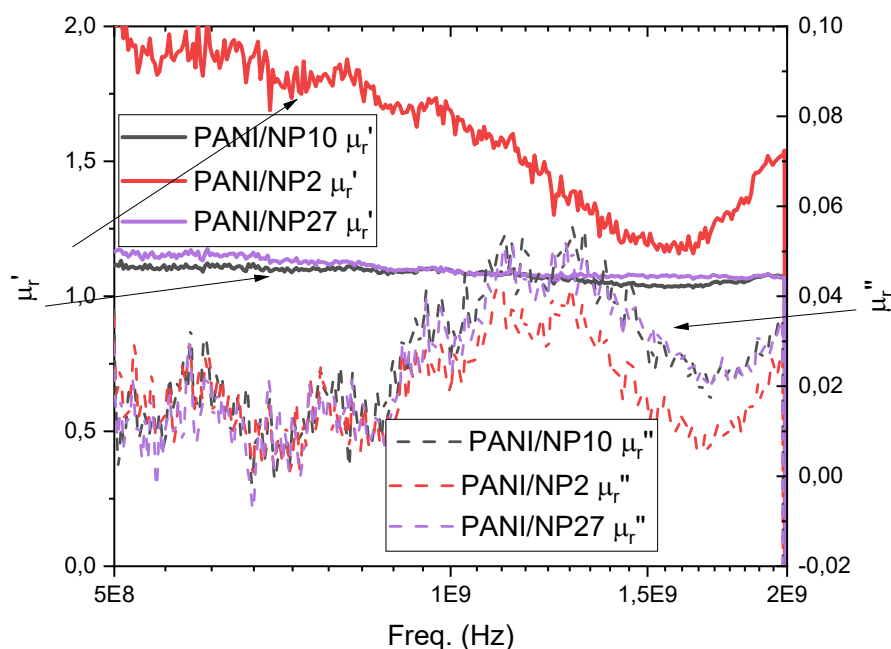
514

515 **Figure 7.** Real (ϵ_r') and imaginary (ϵ_r'') part of the relative permittivity of the PANI/Fe₃O₄NPs
 516 composites. The data exhibits a rather flat behavior up to 1 GHz.

517

518 The ac permeability results (Figure 8) show that PANI/NP2, the composite with 2.3 nm single
 519 domain NPs, with vanishing M_{rem} (Table 4) and higher static initial permeability, has the highest
 520 real part of permeability also in ac. The other samples show relative permeabilities just slightly
 521 above 1. All composites display a wide frequency peak of the imaginary part of the
 522 permeability, which starts below 1 GHz and has a peak at 1.1-1.2 GHz, depending on the
 523 composite, clearly showing that ac losses are only associated to the ferromagnetic resonance.
 524 The large peak width reflects the distribution of particle dimensions and magnetic properties
 525 (also due to exact size, chemical composition, etc.). These results, while compatible with
 526 previous literature (Yun *et al.*, 2014), extend the experimental frequency range explored and
 527 prove that PANI composites with very small Fe oxide particles are instrumental to the
 528 successful use of these materials as energy absorbers in the GHz range.

529



530

531 **Figure 8.** Real (μ_r') and imaginary (μ_r'') part of the relative permeability of the samples. μ_r''
 532 shows an absorption behavior, due to the ferromagnetic resonance, at frequencies slightly above
 533 1 GHz.

534

535

536

Conclusions

537 We have shown that magnetite NPs spanning the size range from 2.3 to 27 nm are able to
 538 catalyze the oxidative polymerization of the aniline dimer and remain within the polymer so to
 539 form PANI/Fe₃O₄ composites. The yields are in all cases high enough to be of practical
 540 importance. Their dependence on the NP surface area shows that i) the NPs are stable against
 541 aggregation in the reaction conditions, ii) the catalytic effect is due to the NPs (and not to Fe³⁺
 542 ions leached into the aqueous phase), and iii) the NPs are a main factor affecting the
 543 polymerization yield. The smallest NPs seem to be not completely stable in the reaction
 544 conditions probably because of their very high surface area that makes them more sensitive to
 545 surface effects such as aggregation and degradation. The embedded NPs retain the shape and
 546 size of the pristine NPs and are well-dispersed in the PANI matrix.

547 The NPs in the composite do not interact by direct exchange, *i.e.*, they retain their magnetic
 548 individuality thanks to the oleic acid coating that prevents direct contact between the NPs. This
 549 enables easy modulation of the composite magnetic properties based on the NP size. Occurrence
 550 of NP direct contact in the composite would have led to unpredictable magnetic properties

depending on the details of the polymerization. For the dynamic electromagnetic behavior, the imaginary part of the permeability only shows an absorption, not associated with any dielectric loss, but rather due to the ferromagnetic resonance, at frequencies slightly above 1 GHz. Our synthetic method thus provides a pathway to prepare composites with tailored magnetic properties by customizing the size of the magnetite NPs. It would also be conceivable to prepare composites containing NPs with different size in controlled proportion.

Funding. Financial support from Fondazione Cariplo (Milano, Italy) under Grant no. 2012-0872 (Magnetic-nanoparticle-filled conductive polymer composites for EMI reduction) is gratefully acknowledged.

Conflict of interest. The authors declare no conflict of interest.

Supplementary data

Electronic Supplementary Material associated with this article can be found in the online version of this paper (DOI: xxxxxxxxxx).

References

- Ahmadkhani L, Mostafavi E, Ghasemali S, Baghban R, Pazoki-Toroudi H, Davaran S, Malakootikhah J, Asadi N, Mammadova L, Saghfi S, Webster TJ, Akbarzadeh A (2019) Development and characterization of a novel conductive polyaniline-g-polystyrene/Fe₃O₄nanocomposite for the treatment of cancer. *Artif Cells Nanomed Biotechnol* 47(1):873-881. doi: 10.1080/21691401.2019.1575839
- Bhadra S, Khastgir D, Singha NK, Lee JH (2009) Progress in preparation, processing and applications of polyaniline. *Prog Polym Sci* 34:783–810. doi: 10.1016/j.progpolymsci.2009.04.003
- Barbaro D, Di Bari L, Gandin V, Evangelisti C, Vitulli G, Schiavi E, Marzano C, Ferretti AM, Salvadori P (2015) Glucose-coated superparamagnetic iron oxide nanoparticles prepared by metal vapour synthesis are electively internalized in a pancreatic adenocarcinoma cell line expressing GLUT1 transporter *Plos One* 10:e0123159. doi: 10.1371/journal.pone.0123159

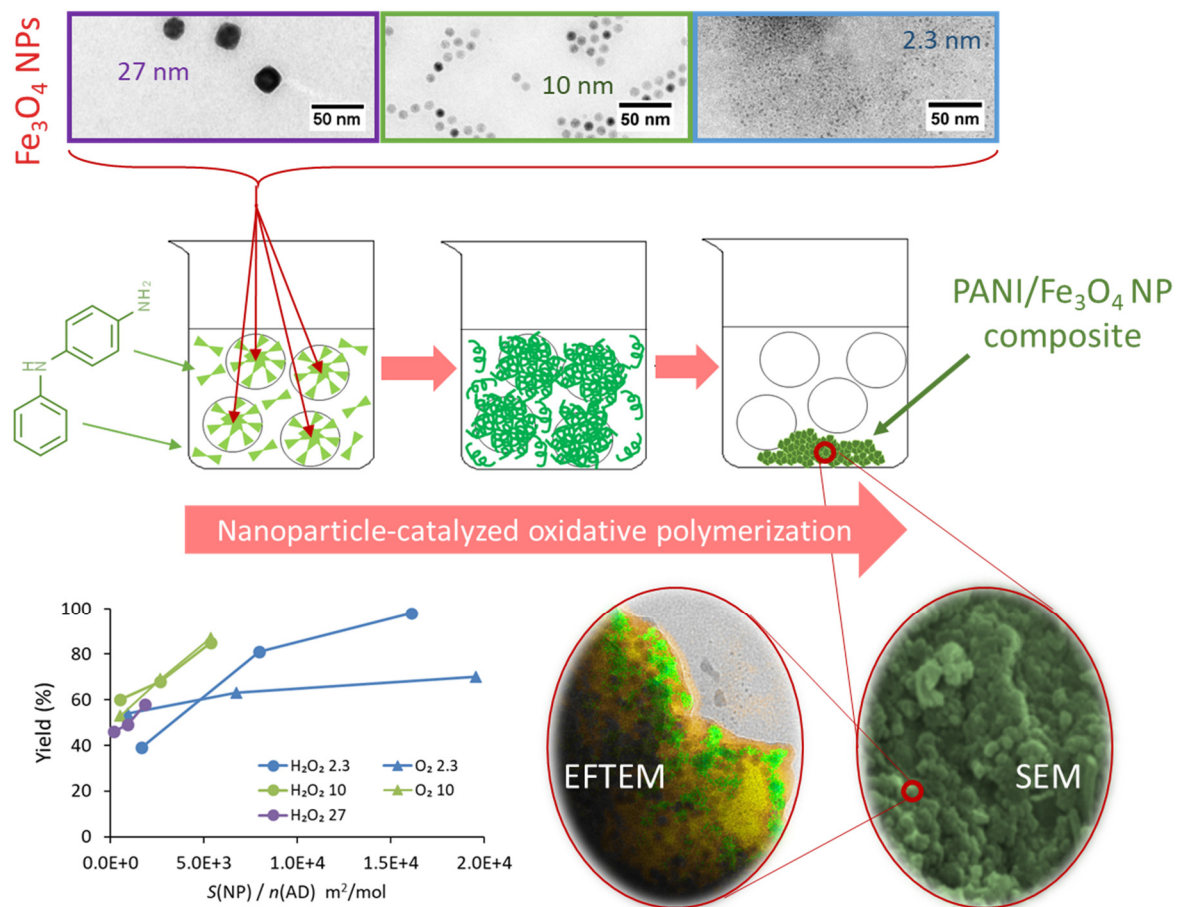
- 585 Bruvera IJ, Mendoza Zélis P, Pilar Calatayud M, Goya GF, Sánchez FH (2015) Determination
586 of the blocking temperature of magnetic nanoparticles: The good, the bad, and the
587 ugly. *J Appl Phys* 118:184304. doi:10.1063/1.4935484
- 588 Campisi S, Palliggiano S, Gervasini A, Evangelisti C (2019) Finely Iron-Dispersed Particles on
589 beta Zeolite from Solvated Iron Atoms: Promising Catalysts for $\text{NH}_3\text{-SCO}$. *J Phys*
590 *Chem C* 123:11723-11733. doi: 10.1021/acs.jpcc.9b01474
- 591 Coey JMD (2010) *Magnetism and Magnetic Materials*, Cambridge, Cambridge University
592 Press, p. 266.
- 593 Della Pina C, Rossi M, Ferretti AM, Ponti A, Lo Faro M, Falletta E (2012) One-pot synthesis
594 of polyaniline/ Fe_3O_4 nanocomposites with magnetic and conductive behaviour.
595 Catalytic effect of Fe_3O_4 nanoparticles. *Synth Met* 162:2250-2258. doi:
596 10.1016/j.synthmet.2012.10.023; Della Pina C, Falletta E, Ferretti AM, Ponti A,
597 Gentili GG, Verri V, Nesti R (2014) Microwave characterization of magnetically hard
598 and soft ferrite nanoparticles in K-band. *J Appl Phys* 116:154306.
599 doi:10.1063/1.4898138; Della Pina C, Ferretti AM, Ponti A, Falletta E (2015) A green
600 approach to magnetically-hard electrically-conducting polyaniline/ CoFe_2O_4
601 nanocomposites. *Compos Sci Technol* 110:138-144. doi:
602 10.1016/j.compscitech.2015.02.007; Della Pina C, De Gregorio MA, Clerici L,
603 Dellavedova P, Falletta E (2018) Polyaniline (PANI): an innovative support for
604 sampling and removal of VOCs in air matrices. *J Hazard Mater* 344:1-8. doi:
605 10.1016/j.jhazmat.2017.10.012
- 606 Dong H, Hu W (2012) *Conducting Polymers: Applications in Electronics and Photovoltaics in*
607 *Book: Encyclopedia of Radicals in Chemistry, Biology and Materials*, Publisher: John
608 Wiley and Sons.
- 609 Evangelisti C, Schiavi E, Aronica LA, Psaro R, Balerna A, Martra G (2015) Solvated Metal
610 Atoms in the Preparation of Supported Gold Catalysts. In: Prati L, Villa A (eds), *Gold*
611 *Catalysis: Preparation, Characterization and Applications*, Jenny Stanford Publishing,
612 Beijing, PRC.
- 613 Falletta E, Ponti A, Sironi A, Ferretti AM, Della Pina C (2015) Nanoferrites as Catalysts and
614 Fillers for Polyaniline/Nanoparticle Composites Preparation. *J Adv Catal Sci Technol*
615 2:8-16. doi: 10.15379/2408-9834.2015.02.02.02
- 616 Ferretti AM, Usseglio S, Mondini S, Drago C, La Mattina R, Chini B, Verderio C, Leonzino
617 M, Cagnoli C, Joshi P, Boraschi D, Italiani P, Li Y, Swartzwelter BJ, Sironi L, Gelosa
618 P, Castiglioni L, Guerrini U, Ponti A (2021) Towards bio-compatible magnetic

- nanoparticles: Immune-related effects, in-vitro internalization, and in-vivo bio-distribution of zwitterionic ferrite nanoparticles with unexpected renal clearance. *J Coll Interf Sci* 582:678-700. doi:10.1016/j.jcis.2020.08.026.
- Fiorillo F (2010) Measurements of magnetic materials. *Metrologia* 47:S114–S142. doi:10.1088/0026-1394/47/2/S11
- Hyeon T, Lee SS, Park J, Chung Y, Na H B (2001) Synthesis of highly crystalline and monodisperse maghemite nanocrystallites without a size-selection process. *J Am Chem Soc* 123:12798–12801. doi:10.1021/ja016812s
- Ibanez JG, Rincón ME, Gutierrez-Granados S, Chaha M, Jaramillo-Quintero OA, Frontana-Uribe BA (2018) Conducting Polymers in the Fields of Energy, Environmental Remediation, and Chemical–Chiral Sensors. *Chem Rev* 118(9):4731-4816. doi:10.1021/acs.chemrev.7b00482
- Kaur G, Adhikari R, Cass P, Bown M, Gunatillake P (2015) Electrically conductive polymers and composites for biomedical applications. *RSC Adv* 5:37553-37567. doi:10.1039/C5RA01851J
- Li J, Qiao J, Lian K (2020) Hydroxide ion conducting polymer electrolytes and their applications in solid supercapacitors: A review. *Energy Stor. Mater* 24:6-21. doi:10.1016/j.ensm.2019.08.012
- Mišurović J, Mojović M, Marjanović B, Vulić P, Ćirić-Marjanović G (2019) Magnetite nanoparticles-catalysed synthesis of conductive polyaniline. *Synth Met* 257:116174(1-11). doi:10.1016/j.synthmet.2019.116174
- Mondini S, Ferretti AM, Puglisi A, Ponti, A (2012) PEBBLES and PEBBLEJUGGLER: Software for Accurate, Unbiased, and Fast Measurement and Analysis of Nanoparticle Morphology from Transmission Electron Microscopy (TEM) Micrographs. *Nanoscale* 4:5356-5372. doi:10.1039/C2NR31276J
- Mondini S, Leonzino M, Drago C, Ferretti AM, Usseglio S, Maggioni D, Tornese P, Chini B, Ponti A (2015) Zwitterion-Coated Iron Oxide Nanoparticles: Surface Chemistry and Intracellular Uptake by Hepatocarcinoma (HepG2) Cells. *Langmuir* 31:7381–7390. doi:10.1021/acs.langmuir.5b01496
- Movassagh-Alanagh F, Bordbar-Khiabani A, Ahangari-Asl A (2017) Three-phase PANI@nano-Fe₃O₄@CFs heterostructure: Fabrication, characterization and investigation of microwave absorption and EMI shielding of PANI@nano-Fe₃O₄@CFs/epoxy hybrid composite. *Compos Sci Technol* 150:65-78. doi:10.1016/j.compscitech.2017.07.010

- Muhammad A, Shah AHA, Bilal S, Rahman G (2019) Basic Blue Dye Adsorption from Water Using Polyaniline/Magnetite (Fe_3O_4) Composites: Kinetic and Thermodynamic Aspects. *Materials*, 12:1764(1-26). doi: 10.1039/C7SE00139H10.3390/ma12111764
- Park J, An K, Hwang Y, Park J-G, Noh H-J, Kim J-Y, Park J-H, Hwang N-M, Hyeon T (2004) Ultra-large-scale syntheses of monodisperse nanocrystals. *Nature Mater* 3:891–895. doi:10.1038/nmat1251
- Qiu G, Wang Q, Nie M (2006) Polyaniline/ Fe_3O_4 Magnetic Nanocomposite Prepared by Ultrasonic Irradiation. *J Appl Polym Sci* 102:2107-2111. doi: 10.1002/app.24100
- Tzou K, Gregory RV (1992) Kinetic study of the chemical polymerization of aniline in aqueous solutions. *Synth Met* 47:267-277. doi:10.1016/0379-6779(92)90367-R
- Wang X, Liu Y, Han H, Zhao Y, Mad W, Sun H (2017) Polyaniline coated Fe_3O_4 hollow nanospheres as anode materials for lithium ion batteries. *Sustain. Energy Fuels* 1:915-922. doi: 10.1039/C7SE00139H
- Wang Y, Liu A, Han Y, Li T (2020) Sensors based on conductive polymers and their composites: a review. *Polym Int*, 69:7–17. doi:10.1002/pi.5907
- Wońska M, Szczytko J, Majhofer A, Gosk J, Działkowski K, Twardowski A (2013) Magnetic interactions in an ensemble of cubic nanoparticles: A Monte Carlo study. *Phys Rev B* 88:144421. doi:10.1103/PhysRevB.88.144421
- Yang C, Zhang P, Nautiyal A, Li S, Liu N, Yin J, Deng K, Zhang X (2019) Tunable Three-Dimensional Nanostructured Conductive Polymer Hydrogels for Energy-Storage Applications. *ACS Appl Mater Interfaces* 11(4):4258-4267. doi: 10.1021/acsami.8b19180
- Yun H, Liu X, Paik T, Palanisamy D, Kim J, Vogel WD, Viescas AJ, Chen J, Papaefthymiou GC, Kikkawa JM, Allen MG, Murray CB (2014) Size- and Composition-Dependent Radio Frequency Magnetic Permeability of Iron Oxide Nanocrystals. *ACS Nano* 8:12323-12337. doi:2481/10.1021/nn504711g.

681 **Graphical Abstract**

682



683

684

685